[1] Dep. App. Mathematics III, Laboratori de Càlcul Numèric (LaCàN), Universitat Politècnica de Catalunya (UPC), Spain. [2] Centre for Geotechnical and Materials Modelling, University of Newcastle, Australia

**Abstract**

This study extends the limit analysis techniques used for the computation of strict bounds of the load factors in solids to stability problems with interfaces, anchors and joints. The cases considered include the pull-out capacity of multi-belled anchors and the stability of retaining walls for multiple conditions at the anchor/soil and wall/soil interfaces. Three types of wall supports are examined: free standing wall, simply supported wall and anchored wall. The results obtained are compared against available experimental and numerical data. The conclusion drawn confirms the validity of numerical limit analysis for the computation of accurate bounds on limit loads and capturing failure modes of structures with multiple inclusions of complex interface and support conditions.

# Stability of anchored sheet wall in cohesive-frictional soils by FE limit analysis

J J Muñoz[1], A V Lyamin[2] and A Huerta[1]

February 12, 2012

## 1 Introduction

The use of anchored structures is a widespread engineering practice. Applications to mention are the anchoring of retaining walls, protection against rock-fall or tower toppling, or stabilisation of caverns and tunnels [32, 23]. However, the design and stability analysis of such structures relies (i) on the national regulations, which may vary among countries, as it is acknowledged in BS EN 1537:2000 standard, (ii) on experimental results, or on (iii) assumed failure mechanism of simplified geometries [2, 20, 21, 27, 28, 26]. Usually, uniform load transfer from grout to ground and cylindrical or conical failure surface around the anchor are assumed. The anchor may be also considered as a fixed point with an applied traction on the wall, and a straight failure line is often assumed as a wall failure mechanism with a Coulomb friction law. As it will be shown later in the paper, this may not be the case when the soil weight is taken into account.

During last decades, the efficient numerical formulations of the lower and upper bound theorems of classical plasticity theory have allowed scientists and engineers to estimate [34] or obtain the strict bounds [14]-[19] for some academic examples such as the bearing capacity of foundations or the analysis of a single- and double-bell anchors [8, 10].

The paper presents some extensions of these formulations that will permit to estimate the pull-out capacity of the grouting and to model the overall anchored wall system in two dimensions. These problems require the inclusion of the interface conditions, and the modelling of the tie which may in turn require the simulation of joints at the tie end. Therefore, the description of how such features are incorporated in the discrete formulations developed so far is included in the scope of the paper.

The flow of the paper proceed as follows. Section 2 presents the core lower and upper bound formulations used in the computations. In Section 3 the necessary extensions dealing with interface modelling are introduced, and in Section 4 they are applied to analyse the pull-out capacity of anchors and the stability of retaining walls. The obtained results are then compared to the outcomes of previously conducted experimental and numerical studies.

## 2 Lower and upper bound formulations

The discretised form of the limit analysis problem are presented next for completeness. The discrete spaces coincide with those given in [6, 13, 14, 15, 19]. The reader familiar with these references may skip this section.

## 2.1 Lower bound formulation

In the following, it will be assumed that the failure mechanism of a body $\Omega$ includes some continuous deformation and a set of discontinuities at some internal boundaries $\Gamma$. The body is subjected to surface loads $\lambda \boldsymbol{g}$ and body loads $\lambda \boldsymbol{f}$, with $\lambda$ being the load factor. Its maximum value $\lambda^*$ that the body can bear without collapsing can be obtained by solving the following maximisation problem:

$$\begin{aligned} \lambda^* = & \max_{\lambda, \boldsymbol{\sigma} \in \mathcal{B}} \lambda \\ & s.t. \begin{cases} a(\boldsymbol{v}, \boldsymbol{\sigma}) + b(\boldsymbol{v}, \boldsymbol{\sigma}) = \lambda \ell(\boldsymbol{v}), \quad \forall \boldsymbol{v} \\ \boldsymbol{\sigma} \in \mathcal{B} \end{cases} \end{aligned} \tag{1}$$

which corresponds to the lower bound theorem of limit analysis [5, 4]. The bilinear forms $b(\boldsymbol{v}, \boldsymbol{\sigma})$ and $a(\boldsymbol{v}, \boldsymbol{\sigma})$ represent respectively the dissipation power at the discontinuity $\Gamma$ and at the remaining domain $\Omega$. The linear form $\ell(\boldsymbol{v})$ is the power of the external forces. The three quantities are explicitly defined by

$$\begin{aligned} a(\boldsymbol{v}, \boldsymbol{\sigma}) &:= \int_{\Omega \setminus \Gamma} \boldsymbol{\varepsilon}(\boldsymbol{v}) : \boldsymbol{\sigma} \mathrm{d}\Omega \\ b(\boldsymbol{v}, \boldsymbol{\sigma}) &:= \int_{\Gamma} [\![\boldsymbol{v}]\!] \cdot \boldsymbol{\sigma} \boldsymbol{n} \mathrm{d}\Gamma = \int_{\Gamma} [\![\boldsymbol{v}]\!] \bar{\otimes} \boldsymbol{n} : \boldsymbol{\sigma} \mathrm{d}\Gamma \\ \ell(\boldsymbol{v}) &:= \int_{\Omega} \boldsymbol{v} \cdot \boldsymbol{f} \mathrm{d}\Omega + \int_{\partial\Omega} \boldsymbol{v} \cdot \boldsymbol{g} \mathrm{d}\Gamma, \end{aligned} \tag{2}$$

where the operator $\bar{\otimes}$ is a symmetrised dyadic product: $\boldsymbol{a} \bar{\otimes} \boldsymbol{b} = \frac{1}{2}(\boldsymbol{a} \otimes \boldsymbol{b} + \boldsymbol{b} \otimes \boldsymbol{a})$. The normal vector $\boldsymbol{n}$ at any point $\boldsymbol{x} \in \Gamma$ located between domains $\Omega^e$ and $\Omega^{e'}$ points from $\Omega^e$ towards $\Omega^{e'}$, while $[\![\boldsymbol{v}]\!] = \boldsymbol{v}^{e'} - \boldsymbol{v}^e$ denotes the velocity jump at this point.

A discrete version of the maximisation problem in (1), which provides a lower bound $\lambda^{LB}$ of $\lambda^*$ may be obtained by using a feasible sub-space of the stress field [14, 19] that satisfies the conditions in (1), that is, a statically admissible stress field, denoted

by $\boldsymbol{\sigma}^{LB}$. A common choice is to use piecewise linear stresses defined on a mesh with $N_e$ triangles (tetrahedra in 3D). Figure 1a schematises the spaces $\boldsymbol{\sigma}^{LB}$ for two adjacent elements that have been shrunk to ease the visualisation of discontinuous fields. The squares in Figure 1a denote the nodal stress values, while the circles indicate nodal velocities (element-wise constant at the element interior, and linear at the edges). The latter are actually the Lagrange multipliers associated with the equilibrium conditions in (1), which are then enforced at the element interiors, at the the Neumann boundaries, and at each one of the $N_\xi$ internal boundaries (edges in 2D, faces in 3D). In compact form these equilibrium conditions read,

$$\begin{aligned} &\lambda^* = \max \lambda \\ &s.t. \begin{cases} \mathbf{A}\boldsymbol{\sigma}^{LB} + \lambda \mathbf{f} = \mathbf{0} \\ \boldsymbol{\sigma}_i^{LB,e} \in \mathcal{B}, \qquad e = 1, \ldots, N_e, i = 1, \ldots, n_{sd}+1 \end{cases} \end{aligned} \tag{3}$$

The stress $\boldsymbol{\sigma}^{LB}$ is the result of assembling all the $n_{sd}+1$ nodal values $\boldsymbol{\sigma}_i^{LB,e}$ for each element $e$, with $n_{sd}$ being the number of space dimensions. Matrix $\mathbf{A}$ is the result of assembling all equilibrium conditions.

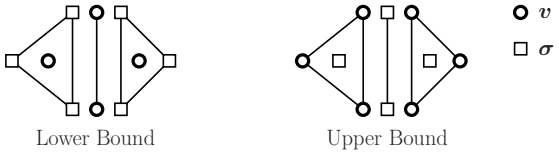


Figure 1: Discrete spaces considered for the lower and upper bound. Symbols at vertices indicate nodal values of piecewise linear spaces, while symbols in the middle of triangles indicate piecewise constant spaces.

## 2.2 Upper bound formulation

The optimal value $\lambda^*$ may be also found as the result of the following minimisation problem, dual to problem (1):

$$\lambda^* = \min_{\boldsymbol{v}} D(\boldsymbol{v}) \quad s.t. \begin{cases} \ell(\boldsymbol{v}) = 1 \\ -\boldsymbol{\varepsilon}(\boldsymbol{v}) \in \mathcal{B}^* \\ -[\![\boldsymbol{v}]\!] \bar{\otimes} \boldsymbol{n} \in \mathcal{B}^* \end{cases} \tag{4}$$

The dissipation power $D(\boldsymbol{v})$ is defined as $D(\boldsymbol{v}) = \max_{\boldsymbol{\sigma} \in \mathcal{B}} (a(\boldsymbol{v}, \boldsymbol{\sigma}) + b(\boldsymbol{v}, \boldsymbol{\sigma}))$, whose expression solely depends on the strain rates and velocity jumps and is well known for classical plasticity criteria [7]. The set $\mathcal{B}^*$ is the dual cone to the set $\mathcal{B}$, defined by $\mathcal{B}^* = \{\boldsymbol{z} | \boldsymbol{z} : \boldsymbol{\sigma} \geq 0, \forall \boldsymbol{\sigma} \in \mathcal{B}\}$, so that the membership conditions in (4) are equivalent to the usual associative rule of the strain rates and velocity jumps.

A discrete version of the problem above that allows computing an upper bound $\lambda^{UB} > \lambda^*$ may be then obtained by using a normalised velocity field $\boldsymbol{v}^{UB}$ such that $\ell(\boldsymbol{v}^{UB}) = 1$ and is everywhere kinematically admissible, i.e. satisfies the membership conditions in (4). A common choice [6, 13, 15, 19] is the use of a piecewise linear velocity field, as shown in Figure 1. The associated Lagrange multipliers to the membership conditions in (4) represent a set of piecewise constant stresses $\boldsymbol{\sigma}^{UB}$ inside the elements and linear stresses $\boldsymbol{s}^{UB}$ at the edges, while the Lagrange multiplier corresponding to constraint $\ell(\boldsymbol{v}^{UB}) = 1$ is the load factor $\lambda^{UB}$ [6, 19]. After inserting the

aforementioned discretisation in equation (4), this dual problem turns into,

$$\lambda^* = \min_{\boldsymbol{v}} D(\boldsymbol{v}^{UB})$$
$$s.t. \begin{cases} \ell(\boldsymbol{v}^{UB}) = 1 \\ -\boldsymbol{\varepsilon}(\boldsymbol{v}_i^{UB,e}) \in \mathcal{B}^*, \quad e = 1, \ldots, N_e, i = 1, 2 \\ -[\![\boldsymbol{v}^{UB}]\!]_i^{\xi} \bar{\otimes} \boldsymbol{n}^{\xi} \in \mathcal{B}^*, \quad \xi = 1, \ldots, N_{\xi}, i = 1, 2 \end{cases} \tag{5}$$

where $\boldsymbol{v}_i^{UB,e}$ denotes the velocity vector at node $i$ of element $e$, and $[\![\boldsymbol{v}^{UB}]\!]_{\xi}$ is the velocity jump at node $i$ of edge $\xi$.

For some common plasticity criteria such as von Mises or two-dimensional Mohr-Coulomb criteria, the set defining the admissible stresses $\mathcal{B}$ in (3) and (5) may be replaced (using convenient linear transformations of the stresses $\boldsymbol{\sigma}^{LB}$ and $\boldsymbol{\sigma}^{UB}$ [6, 9, 15, 16, 19]) by a Lorentz cone $\mathcal{L}$ defined by $\mathcal{L} := \{\boldsymbol{x} \in \mathbb{R}^n | x_1 \geq \|\{x_2, \ldots, x_n\}\|\}$, which allows to solve the problem above resorting to second order conic programming (SOCP) software [12, 29, 30]. The results in Section 4 have employed such transformations.

## 2.3 Mesh adaptivity

The resulting optimal variables of the lower and upper bound problems, $(\boldsymbol{\sigma}^{LB}, \boldsymbol{v}^{LB})$ and $(\boldsymbol{\sigma}^{UB}, \boldsymbol{v}^{UB})$ may be combined to compute elemental and edge contributions to the total load gap $\Delta\lambda = \lambda^{UB} - \lambda^{LB}$, denoted respectively by $\Delta\lambda^e$ and $\Delta\lambda^{\xi}$, and defined

by:

$$\Delta\lambda^e = \int_{\Omega^e} \boldsymbol{\sigma}^{UB,e} : \boldsymbol{\varepsilon}(\boldsymbol{v}^{UB}) d\Omega + \int_{\Omega^e} \nabla \cdot \boldsymbol{\sigma}^{LB} \cdot \boldsymbol{v}^{UB} d\Omega - \int_{\partial\Omega^e} \boldsymbol{\sigma}^{LB} \boldsymbol{n} \cdot \boldsymbol{v}^{UB} d\Gamma$$
$$\Delta\lambda^\xi = \int_{\Gamma^\xi} \boldsymbol{s}^{UB,\xi} \cdot [\![\boldsymbol{v}^{UB}]\!] d\Gamma - \int_{\Gamma^\xi} \boldsymbol{\sigma}^{LB} \boldsymbol{n} \cdot [\![\boldsymbol{v}^{UB}]\!] d\Gamma \tag{6}$$

These gap contributions satisfy the properties $\Delta\lambda = \sum_e \Delta\lambda^e + \sum_\xi \Delta\lambda^\xi$, $\Delta\lambda^e \geq 0$ and $\Delta\lambda^\xi \geq 0$ [6, 19], which allows us to use these quantities in a mesh adaptivity process: those elements and edges that have larger contributions will be remeshed in order to successively reduce the total gap $\Delta\lambda$ and hence capture more accurately the collapse mechanism.

# 3 Including interfaces, duplicated edges and joints

This paper aims to extend the previous formulation to more realistic situations encountered in common structures of civil engineering, without relaxing the strictness of the bounds. For this reason, the necessary changes that each one of these situations must include for the lower and upper bound formulations will be described and justified separately. These changes do respect the construction of statically and kinematically admissible spaces in each case, and allow to employ the same refinement process described in Section 2.3 for the extended problem.

## 3.1 Interface conditions

The presented formulations will be extended next to problems with specific frictional conditions at interfaces that separate two different materials. In the examples consid-

ered in this paper, these correspond to wall-soil and grouting-soil interactions. For clarity these extensions are described for two-dimensional analysis, but they can be easily generalised to three-dimensional problems.

### 3.1.1 Lower bound

Let us consider two triangular elements, $A$ and $B$, with different material properties. In this case, additional yield criteria at the interface and equilibrium conditions between the interface and the elements must be included. This is accomplished by adding an edge $I$ between elements $A$ and $B$, with nodal stresses $\boldsymbol{\sigma}_1^I$, $\boldsymbol{\sigma}_2^I$, as represented with squares in Figure 2a. The optimisation problem is then complemented with (i) membership conditions for the new nodes of the edge , and (ii) equilibirum condition between one of the elements, for instance element $A$, and the inserted edge $I$. Due to the equilibrium condition between element $A$ and $B$, the equibrium between element $B$ and interface $I$ is ensured. More specifically, point (i) is defined as a membership condition for the two additional nodal stress variables $\boldsymbol{\sigma}_1^I, \boldsymbol{\sigma}_2^I$ as,

$$\boldsymbol{\sigma}_i^I \in \mathcal{B}_I, \quad i = 1, 2 \tag{7}$$

with $\mathcal{B}_I$ being the set of admissible stresses at the interface, while the equilibrium conditions between elements and those in point (ii) read

$$(\boldsymbol{\sigma}_i^A - \boldsymbol{\sigma}_i^B)\boldsymbol{n} = \mathbf{0}, \quad i = 1, 2 \tag{8}$$

$$(\boldsymbol{\sigma}_i^A - \boldsymbol{\sigma}_i^I)\boldsymbol{n} = \mathbf{0}, \quad i = 1, 2 \tag{9}$$

The nodal velocities at the two edges between $A$ and $B$, indicated in Figure 2a with circles, correspond in fact to the Lagrange multipliers associated with these constraints:

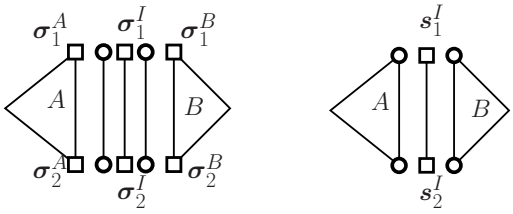


(a) (b)

Figure 2: Discrete spaces considered for the lower (a) and upper (b) bound problems when modelling interfaces.

the velocities at one edge are associated with equation (8) while those at the other edge correspond to equation (9).

Some examples of the admissible normal and shear components of the tractions that will be used in the results section are given in Figure 3. It is worth noting that by using suitable transformation of $\boldsymbol{\sigma}_i^I$, all of them can be defined as second order cones with additional constraints in cases (b) and (d). More specifically, for each case shown in Figure 3 set $\mathcal{B}_I$ is equal to:

$$(a)\ \text{Mohr-Coulomb} \quad ; \quad (c)\ \text{von Mises with } \sigma_Y \approx 0$$

$$(b) \begin{cases} \text{Mohr-Coulomb} \\ \boldsymbol{n} \cdot \boldsymbol{\sigma}_i^I \boldsymbol{n} \leq 0 \end{cases} \quad ; \quad (d) \begin{cases} \text{von Mises with } \sigma_Y \approx 0 \\ \boldsymbol{n} \cdot \boldsymbol{\sigma}_i^I \boldsymbol{n} \leq 0 \end{cases}$$

Set $(a)$ corresponds to standard friction with Coulomb law. Set in $(b)$ is the same as $(a)$, but removing any resistance under tension, and retaining the cohesion at the interface. In this case, the interface can have some non-zero shear component even in the absence of tension. Case $(c)$ corresponds to the case of perfect smooth sliding without shear component, and case $(d)$ is a more realistic sliding case where no tension

is permitted.

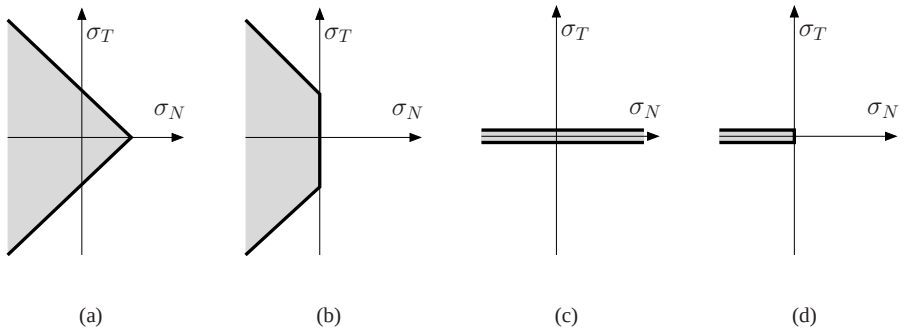


Figure 3: Interface conditions: Rough interface, equal to soil properties (a), Rough with no tension (b), smooth interface (c), and smooth with no tension (d).

### 3.1.2 Upper bound

The upper bound problem uses a set of linear stresses at the edges, which has been denoted by $\boldsymbol{s}^{UB}$. When the edge becomes the interface between two domains, the definition of specific plasticity criteria is achieved by just imposing the interface admissibility set for those stress variables at interface $I$:

$$\boldsymbol{s}_i^{UB,I} \in \mathcal{B}_I, \quad i = 1, 2 \tag{10}$$

Figure 2b depicts by squares the nodal stresses of the interface edge, which replace the stresses at the internal edges between elements $A$ and $B$. Therefore, no additional variables are required in the upper bound formulation. It should be pointed out that the nodal stress $\boldsymbol{s}_i^I$ corresponds in fact to the Lagrange mulitpliers of the associative conditions for the velocity jumps at the interface.

## 3.2 Duplicated edges

In two-dimensional analyses, it may become useful to model two superimposed domains which are connected to a common edge. Those edges that connect two elements on one side, and one element on the other side will be called *duplicated edges*. Figure 4 illustrates this situation, where an element $A$ on the left is connected to elements $B$ and $B'$ on the right. This situation may help to simulate for instance a soil domain with a superimposed tie of an anchor that overlaps the soil without being actually attached to it, but connected to an anchor and to a wall at each end.

### 3.2.1 Lower bound

The equilibrium equation between the three elements $A$, $B$ and $B'$ must equalise the tractions on element $A$ to the sum of the tractions on $B$ and $B'$. Given a vector $\boldsymbol{n}$ normal to the common edge, this equilibrium is equivalent to the following nodal equations:

$$(\boldsymbol{\sigma}_i^A - \boldsymbol{\sigma}_i^B - \boldsymbol{\sigma}_i^{B'})\boldsymbol{n} = \mathbf{0}, i = 1, 2 \tag{11}$$

This equation will be added to the constraints in problem (3). Since there is one equilibrium equation per common node, each duplicated edge requires two nodal velocities, as indicated with circles in Figure 4a. These velocities correspond to the Lagrange multipliers of equations (11).

### 3.2.2 Upper bound

The dissipation power at the edge corresponds to the sum of the power dissipated between elements $A$ and $B$, and the dissipated power between elements $A$ and $B'$. For-

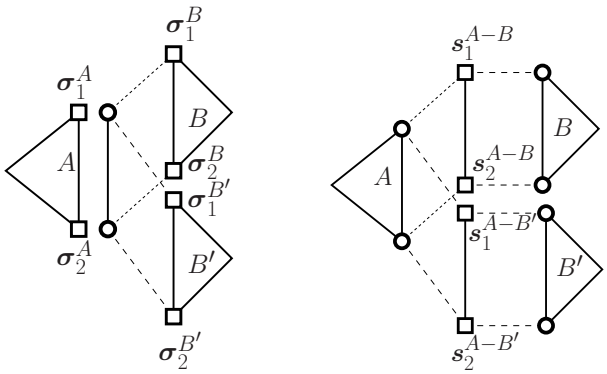


(a) (b)

Figure 4: Discrete spaces considered for the lower (a) and upper (b) bound problems when modelling duplicated edges.

mally, the total dissipation power at the edge correspond to the sum of two integrals along the common edge:

$$b_\xi(\boldsymbol{s},\boldsymbol{v}) = \int_{\Gamma^\xi} \boldsymbol{s}^{A-B}\cdot(\boldsymbol{v}^B-\boldsymbol{v}^A)\mathrm{d}\Gamma + \int_{\Gamma^\xi} \boldsymbol{s}^{A-B'}\cdot(\boldsymbol{v}^{B'}-\boldsymbol{v}^A)\mathrm{d}\Gamma$$

Therefore, each duplicated edge requires two superimposed linear stress spaces, $\boldsymbol{s}^{A-B}$ and $\boldsymbol{s}^{A-B'}$, indicated by two pairs of squares in Figure (4)b. By imposing that each one of the four nodal variables is admissible, that is:

$$\begin{cases} \boldsymbol{s}_i^{A-B} \in \mathcal{B} \\ \boldsymbol{s}_i^{A-B'} \in \mathcal{B} \end{cases}, i=1,2,$$

the admissibility of the corresponding velocity jumps $\boldsymbol{v}_i^A-\boldsymbol{v}_i^B$ and $\boldsymbol{v}_i^A-\boldsymbol{v}_i^{B'}$ is ensured, and therefore the strictness of the upper bound is guaranteed. The nodal velocities are indicated with circles in Figure 4b.

## 3.3 Modelling the joints

In some particular cases, it appears to be convenient to disregard the collapse due to the relative rotation of two domains. For instance, in the examples shown in Section 4.2, the bearing capacity of the tendon of an anchor is modelled as independent of the angle that the tendon adopts with respect to the grouting, or the angle it makes at the wall attachment. This situation corresponds to the modelling of a revolute joint without rotational dissipation, as depicted in Figure 5.

The modelling of such joint is characterised by i) translational equilibrium at the contact point, and ii) a rotation of the adjacent element around a single common point. The conditions in i) and ii) correspond respectively to the lower and the upper bound conditions of admissibility, which will be detailed next.

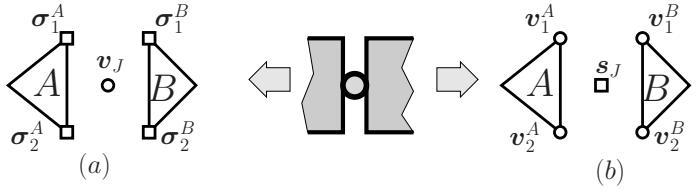


Figure 5: Rotational joint and discrete spaces considered for the lower (a) and upper (b) bound problem.

### 3.3.1 Lower bound

The point-wise or node-to-node equilibrium conditions at the edge between elements $A$ and $B$, which for general continua is contained in equation (3), must be in this case

replaced by the following integral equilibrium equation:

$$\int (\boldsymbol{\sigma}^A - \boldsymbol{\sigma}^B)\boldsymbol{n}\mathrm{d}\Gamma = \mathbf{0}$$

Therefore, instead of imposing equilibrium everywhere along the edge, only the total load at each side of the joint is enforced to be in equilibrium. As a result, a unique Lagrange multiplier or velocity node is defined for such joints, as indicated by $\boldsymbol{v}_J$ in Figure 5a with a single circle, instead of the two circles shown in Figure 1a. The admissibility of the stresses at the joint is given by the admissibility sets of the nodal stresses $\boldsymbol{\sigma}_i^A$ and $\boldsymbol{\sigma}_i^B$. If the yield criteria for these nodal stresses are different from what is set for the tractions at the nodes, then, an additional nodal stress variable is required, with also an additional corresponding equilibrium equation similar to the one considered at the interfaces in eqn. (9).

### 3.3.2 Upper bound

A kinematically admissible field is such that the velocities comply with the joint kinematics, that is, the nodal velocities correspond to two independent rotations around the centre of the joint. Such conditions are imposed by enforcing that the nodal velocity jumps located on the different sides from the centre of the joint (node pairs 1 and 2 in Figure 5b) are equal in magnitude and opposite in sign. Mathematically, this condition reads,

$$[\![\boldsymbol{v}]\!]_1 + [\![\boldsymbol{v}]\!]_2 = \mathbf{0} \tag{12}$$

where $[\![\boldsymbol{v}]\!]_i = \boldsymbol{v}_i^A - \boldsymbol{v}_i^B$ corresponds to the velocity jump at node pair $i$. The constraint in (12) has an associated traction (Lagrange multiplier) that is given by $\boldsymbol{s}_J\boldsymbol{n}$, with $\boldsymbol{s}_J$

being the nodal stress of the joint. The latter has been represented with a single square in Figure 5.

If velocity jumps at the mid-point of the joint are not allowed, the stress tensor $\boldsymbol{s}_J$ is a free variable. If instead, the joint can collapse due to non-admissible tractions, a membership condition $\boldsymbol{s}_J \in \mathcal{B}_J$ must be added. When the kinematic condition in (12) is included, the dissipation energy at the joint is evaluated as,

$$b(\boldsymbol{s}_J, \boldsymbol{v}^{UB}) = \int_{\Gamma^\xi} \boldsymbol{s}_J : (\llbracket \boldsymbol{v} \rrbracket_1 + \llbracket \boldsymbol{v} \rrbracket_2) \bar{\otimes} \boldsymbol{n} d\Gamma$$

### 3.3.3 Joint with multiple elements

After applying the remeshing process described in Section 2.3, the joint conditions described above must be preserved for the whole initial edge defining the joint. In other words, the joint must be equally and uniquely modelled regardless of the number of elements that meet at the joint. In the lower bound problem, a unique velocity node will be always required, and a single equation equalising the stress resultants at each side will be imposed. However, the kinematic condition for the multiple elements requires a set of constraints, such that the velocity jumps at the joint are linear along the joint and zero at its centre, as illustrated in Figure 6. More precisely, if the joint is defined by $N_J$ edges, the following constraints for the velocities must be imposed when solving the upper bound problem:

$$\begin{aligned}
&\llbracket \boldsymbol{v} \rrbracket_1^I = \llbracket \boldsymbol{v} \rrbracket_2^{I-1}, && I = 2, \ldots, N_J \\
&\frac{\llbracket \boldsymbol{v} \rrbracket_1^I}{\llbracket \boldsymbol{v} \rrbracket_2^I} = \frac{\llbracket \boldsymbol{v} \rrbracket_1^{I-1}}{\llbracket \boldsymbol{v} \rrbracket_2^{I-1}}, && I = 2, \ldots, N_J \\
&\llbracket \boldsymbol{v} \rrbracket_1^1 = -\llbracket \boldsymbol{v} \rrbracket_2^{N_J}
\end{aligned}$$

Each one of these $2(N_J - 1) + 1$ vector equations has an associated Lagrange multiplier or stress variable. Consequently, while the lower bound problem requires one single nodal velocity, the upper bound problem will need $2(N_J - 1) + 1$ stress variables. It is also assumed in the numerical examples described in Section 4 that the velocity constraints given above will be satisfied exactly, and that therefore such nodal stresses are unbounded (no dissipation energy will be accounted for).

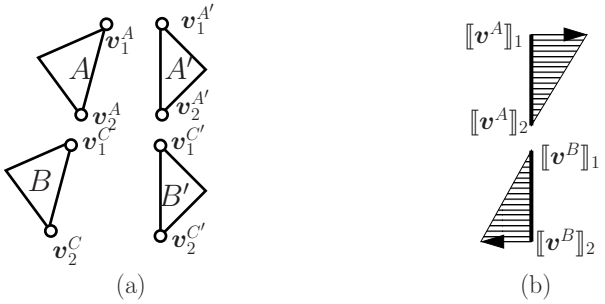


Figure 6: Representation of velocity spaces in upper bound problem (a) and kinematically admissible velocity jumps (b) for joint formed by 2 edges.

# 4 Numerical Results

## 4.1 Pull-out capacity of multi-bell anchors

The pull-out capacity of anchors may be limited by failure i) in the tendon itself (structural failure) ii) at the tendon-grouting interface (slippage), iii) at the grout-ground interface (shear), iv) within the grout column (crushing or bursting), or v) within the soil or rock supporting the bond (interface tendon-grout).

This section studies the dependence of pull-out capacity of horizontal anchors in-

stalled using drilling techniques under a static load. Since the analysis is focused on the anchor-soil interaction, the strength of the grout and tendon are assumed much higher than soil and soil-grouting interface. This effectively means that failure mechanisms i), ii) and iii) above are disregarded.

A comparison has been made between the single- and the double-bell anchors installed in cohesive and cohesive-frictional soils with rough and smooth interfaces. The modelling geometries and FE meshes used for computations are shown in 7. For sand, the ground-grout interface resistance may depend on sand density, permeability and homogeneity [22, 24], while in clays, the boring technique may be determinant [22]. For simplicity, the same interface conditions as those for the soils with some tension limitations shown in Figure 3 are assumed. A reference soil density $\gamma = 1kN/m^3$ and cohesion in clay equal to $c = 1kPa$ are employed.

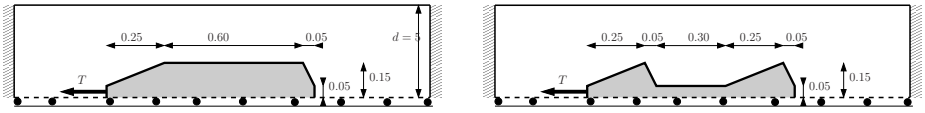


(a) (b)

Figure 7: Geometry and boundary conditions of horizontal anchors with single- and double-bell.

The pull-out capacity of the single- and double-bell anchors are given in Tables 1 and 2, respectively, for different interface conditions and material properties of the soil. No relevant differences in the mechanism and pull-out capacity have been observed when the anchors have been pulled from the left or the right. However, the load capacity decreases in all cases if the interface is smooth. Furthermore, for clay soils, the no-tension condition (indicated by "NT") also reduces the pull-out capacity. Figures 9 and

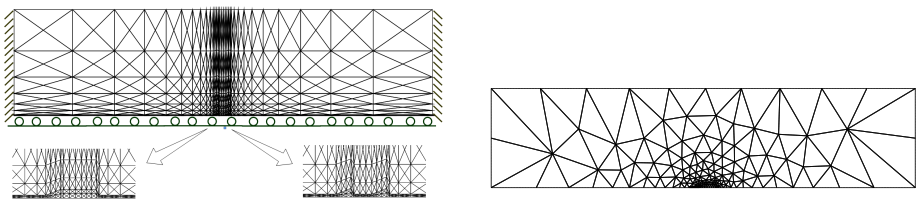

(a) (b)

Figure 8: Typical structured (a) and unstructured (b) FE meshes for anchor pull-out problem.

(a) (b)

Figure 9: Dissipation power at collapse for simple bell anchor in sand with smooth (a) and rough (b) interface conditions.

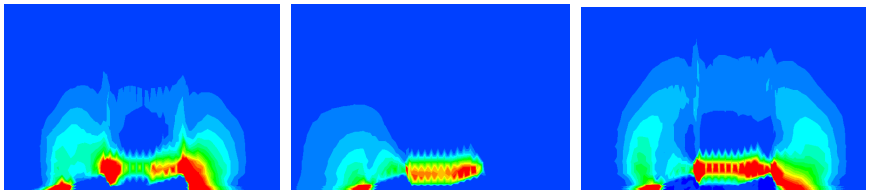

(a) (b) (c)

Figure 10: Dissipation power at collapse for anchor in clay. Interface conditions: smooth (a), cohesive with no tension (b) and fully adhesive (c)

10 show the different mechanisms for sand and clay soils, respectively, using different interface conditions. The latter do not affect the profile of the dissipation power in sand, but they do alter the resulting mechanism in clay.

These results show that the failure mechanisms depend significantly on the material

properties of the soil. For sand material, the slip-lines are extended up to the upper surface (see Figures 11b and 11d), whereas for clay material, and at the modelled depth, the mechanism is localised around the anchor (see Figures 11a and 11c). For the latter case, whether the anchor has one or two bells does not change the results substantially (see Figures 11a and 11c).

In the recent years, several authors have also analysed the pull-out capacity of horizontal and inclined anchors placed on horizontal and sloppy surfaces. This anchors have been analysed using the limit equilibrium method, finite elements [3, 11], or limit analysis [8, 10, 33].

The pull-out capacity in sand soils is measured by the dimensionless factor $F = \frac{p_u}{\gamma d}$, with $\gamma$ being the soil density, $d$ the distance from the anchor to the soil surface, and $p_u = T/B$ the maximum applied pressure, where $T$ is the maximum load and $B$ the width of the anchor. The published studies for a plate anchor [8, 10] did not find substantial differences for rough and smooth soil. Based on results obtained in those references the following formula has been suggested:

$$F = 1 + \frac{d}{B}\tan(\phi) \tag{13}$$

In contrast, the results obtained in the present study suggest a strong dependence of the pull-out capacity of the anchor on the soil-grouting interface. This is probably due to the different shapes of the anchors considered and the difference in pull-out direction. Nonetheless, the values of factor $F$ obtained from the results given in Tables 1, 2 for $d = 5$, $B = 0.3$, $\gamma = 1$ are summarised in Table 3. It should be noted that the values of $F$ obtained are between $2$ and $4$ times higher than those furnished by formula (13), probably due to differences in the geometry and the boundary conditions.

The pull-out capacity in clays has been analysed for instance in [17, 18, 33], and has been expressed as a function of the so-called dimensionless breakdown factor $N_c$ as $T = A\, c\, N_c$, with $A$ being the area of the anchor and $c$ the shear strength of the clay. The resulting values of $N_c$ obtained in this study are also given in Table 3 for the clay material. The factor $N_c$ may be computed using the following formula [18]:

$$N_c = N_{c0} + \frac{\gamma d}{c} \tag{14}$$

with $N_{c0} = \frac{T}{Ac}\Big|_{\gamma=0}$. For vertical plates in uniform clays and for $d/B > 10$, the authors in [18] obtained the value $N_{c0} = 11.86$, which is somehow comparable to $N_c = 16.86$ obtained herein. This value agrees with the smooth and double-bell case, but slightly disagrees with the other cases. Nonetheless, since the anchor geometry used in this study does not correspond to a plate anchor, it is not expected that formula (14) fully matches the values obtained here. It is also worth pointing out that the number of bells has a stronger effect in clay soils than in sand soils.

Tests for London clays have been described in [1], where it is experimentally confirmed that the ultimate load is linearly proportional to the number of bells. It has been verified that such linear relation exists. Figure 12 shows the dissipation power for a three and four bell anchor, together with the pull-out capacity of anchors under different interface conditions as a function of the number of bells. It has been verified that for non-smooth interface conditions, the ultimate capacity depends more strongly on the total length of the anchor than on the number of bells. Interestingly, when the interface conditions are smooth, the geometry of the bells do contribute to the bearing capacity.

| | Clay ($c = 1kPa, \phi = 0°$) | | Sand ($\phi = 20°$) | | Sand ($\phi = 40°$) | |
|---|---|---|---|---|---|---|
| | LB | UB | LB | UB | LB | UB |
| Smooth | 1.70 | 1.75 | 0.88 | 0.93 | 3.38 | 3.76 |
| Smooth + NT | 1.31 | 1.43 | 0.88 | 0.93 | 3.36 | 3.79 |
| Rough | 2.67 | 2.75 | 1.35 | 1.38 | 4.61 | 4.92 |
| Rough + NT | 2.15 | 2.26 | 1.35 | 1.38 | 4.61 | 4.95 |
| NT | 2.23 | 2.32 | 1.35 | 1.40 | 4.61 | 4.91 |

Table 1: Pull-out capacities of horizontal single-bell anchors (for $1/2$ of the anchor). NT=no tension.

| | Clay ($c = 1kPa, \phi = 0°$) | | Sand ($\phi = 20°$) | | Sand ($\phi = 40°$) | |
|---|---|---|---|---|---|---|
| | LB | UB | LB | UB | LB | UB |
| Smooth | 2.32 | 2.43 | 1.01 | 1.06 | 3.51 | 3.88 |
| Smooth + NT | 1.81 | 2.01 | 1.01 | 1.06 | 3.51 | 3.89 |
| Rough | 2.67 | 2.79 | 1.35 | 1.40 | 4.61 | 4.95 |
| Rough + NT | 2.09 | 2.42 | 1.28 | 1.49 | 4.61 | 4.95 |
| NT | 2.23 | 2.34 | 1.35 | 1.41 | 4.61 | 4.96 |

Table 2: Pull-out capacities of horizontal double-bell anchors (for $1/2$ of the anchor). NT=no tension.

| | Single-bell | | | Double-bell | | |
|---|---|---|---|---|---|---|
| | Clay ($N_c$) | $\phi = 20°$ ($F$) | $\phi = 40°$ ($F$) | Clay ($N_c$) | $\phi = 20°$ ($F$) | $\phi = 40°$ ($F$) |
| Smooth | 11.4 | 12.0 | 47.6 | 15.8 | 13.9 | 49.2 |
| Rough | 18.1 | 18.1 | 63.3 | 18.2 | 18.3 | 63.7 |

Table 3: Breakdown factor $N_c = \frac{T}{Ac}$ in clay materials and pull-out capacity factor $F = \frac{T}{B\gamma d}$ in sand. $T$ the double of the average values in Tables 1 and 2.

## 4.2 Stability analysis of retaining wall

The stability of the wall supporting an excavation made in cohesive-frictional soil is investigated in terms of the ratio between the maximum depth of the excavation prior to collapse ($d$) and the total height of the wall ($h$). Figure 13 depicts the three situations considered: (i) a free standing wall, (ii) a simply supported wall, and (iii) an anchored wall. The motivation behind case (ii) is the modelling of one half of a shored retaining wall with intermediate struts.

The same total height $H = 30m$ and width $W = 80m$ of the domain are used in all three cases. These dimensions have been considered large enough so that no special techniques at the boundaries (i.e. [25]) must be used for simulating the infinite domain. The wall embedment depth $h = 16m$ is used everywhere. For each geometry and ratio $d/h$, the limit stability factor $\lambda$, defined as the ratio between the maximum value of the gravity acceleration and the applied value $\|\boldsymbol{g}\| = 23kN/m^3$, that is, $\lambda = \frac{\|\boldsymbol{g}_{max}\|}{\|\boldsymbol{g}\|}$, has been computed. The maximum ratio $d/h$ that a wall can withstand before collapsing corresponds to the case when $\lambda$ approaches 1.

It should be noted that the variable body force $\lambda \boldsymbol{g}$ has been in fact applied to a reduced domain (soil on the right side of the wall), while in the remaining domain a constant weight $\boldsymbol{g}$ is considered. The use of a variable weight in reduced region makes the optimisation problem computationally less expensive than applying the load $\lambda \boldsymbol{g}$ to the whole domain without compromising the accuracy of the analysis.

For the cases considered here, $\|\boldsymbol{g}\| = 23kN/m^3$ is employed, and a soil with cohesion $c = 10kPa$ and internal friction angle $\phi = 22°$. The wall is modelled as a material with a high value of the cohesion ($c = 1e5kPa$), such that no dissipation is detected within the wall. The geometries and assumed boundary conditions for the three systems considered are shown in Figure 13.

#### 4.2.1 Stability of free standing wall

The FE meshes employed for the analysis together with the resulting collapse patterns and dissipation plots are given in Figure (14)a. Table 4 gives the stability factor $\lambda$ described above, where the limit value of $d/h$ that best brackets the bound $\lambda = 1$ has been written in bold.

No substantial difference is detected between the rough and the rough/no tension (rough + NT) conditions. However, the stability ratio $d/h$ is reduced from approximately $0.6$ to $0.488$ if the wall/soil interface is changed from rough to smooth conditions. It canbe deduced therefore that the stability of free standing walls relies significantly on the wall/soil friction.

| W/S Interface = rough | | | | W/S Interface = rough + NT | | | | W/S Interface = smooth | | | |
|---|---|---|---|---|---|---|---|---|---|---|---|
| $d/h$ | LB | UB | Err (%) | $d/h$ | LB | UB | Err (%) | $d/h$ | LB | UB | Err (%) |
| 0.613 | 0.951 | 0.988 | 1.908 | 0.613 | 0.902 | 0.962 | 3.219 | 0.500 | 0.944 | 0.965 | 1.100 |
| **0.606** | 0.981 | 1.016 | 1.753 | 0.606 | 0.953 | 0.994 | 2.106 | 0.494 | 0.964 | 0.995 | 1.582 |
| 0.600 | 1.011 | 1.051 | 1.940 | **0.600** | 0.985 | 1.027 | 2.087 | **0.488** | 1.003 | 1.026 | 1.134 |
| 0.594 | 1.043 | 1.084 | 1.928 | 0.594 | 1.018 | 1.061 | 2.068 | 0.481 | 1.034 | 1.058 | 1.147 |
| 0.588 | 1.076 | 1.118 | 1.914 | 0.588 | 1.052 | 1.096 | 2.048 | 0.475 | 1.067 | 1.091 | 1.112 |
| 0.581 | 1.110 | 1.154 | 1.943 | 0.581 | 1.087 | 1.133 | 2.072 | 0.469 | 1.100 | 1.125 | 1.124 |
| 0.575 | 1.143 | 1.191 | 2.057 | 0.575 | 1.123 | 1.171 | 2.092 | 0.463 | 1.135 | 1.161 | 1.132 |

Table 4: Limit values of the stability factor for different $d/h$ ratios of free standing wall

#### 4.2.2 Stability of simply supported wall

Stability of simply supported retaining wall is assessed in this section. The support which prevents wall from moving horizontally is installed in front of the wall at $h/4$ distance from its top. The vertical movement of the supporting element is not restricted and its attachment to the wall is modelled by moment free joint described in Section 3.3.

The example of the final FE mesh obtained after completion of the adaptive remeshing process together with the resulting collapse patterns and dissipation plots is given in Figure 14b. Additionally, the magnified area of moment-free wall/support joint at collapse is shown in Figure 15a. The collapse load multipliers for the different $d/h$ ratios are given in Table 5. As it can be observed in Figure 14b, the failure mechanism in this case is completely different from the one for the free standing wall. Furthermore,

| W/S Interface = rough | | | | W/S Interface = rough + NT | | | | W/S Interface = smooth | | | |
|---|---|---|---|---|---|---|---|---|---|---|---|
| $d/h$ | LB | UB | Err (%) | $d/h$ | LB | UB | Err (%) | $d/h$ | LB | UB | Err (%) |
| 0.863 | 0.865 | 0.988 | 6.638 | 0.875 | 0.779 | 0.897 | 7.041 | 0.794 | 0.875 | 0.973 | 5.303 |
| 0.856 | 0.910 | 1.036 | 6.475 | 0.869 | 0.822 | 0.941 | 6.750 | 0.788 | 0.910 | 0.962 | 5.356 |
| **0.850** | 0.957 | 1.085 | 6.268 | 0.863 | 0.865 | 0.988 | 6.638 | **0.781** | 0.946 | 1.055 | 5.447 |
| 0.844 | 1.005 | 1.136 | 6.119 | 0.856 | 0.910 | 1.036 | 6.475 | 0.775 | 0.983 | 1.099 | 5.572 |
| 0.838 | 1.055 | 1.189 | 5.971 | **0.850** | 0.957 | 1.085 | 6.268 | 0.769 | 1.021 | 1.144 | 5.681 |
| 0.831 | 1.106 | 1.244 | 5.872 | 0.844 | 1.005 | 1.136 | 6.119 | 0.763 | 1.061 | 1.191 | 5.773 |
| 0.825 | 1.159 | 1.300 | 5.734 | 0.838 | 1.055 | 1.189 | 5.971 | 0.756 | 1.102 | 1.240 | 5.892 |

Table 5: Limit values of the stability factor for different $d/h$ ratios of simply supported wall

from the actual values of the critical ratio $d/h$ in Table 5, it can be concluded that the wall/soil friction does not have such a strong influence on the stability of the simply supported wall, as was observed for the case of the free standing wall.

#### 4.2.3 Stability of anchored wall

Stability of a tied-back retaining wall is investigated. A relatively shallow single-bell anchor is installed at $h/4$ depth, with length and width equal to $1m \times 0.3m$. The full set of problem dimensions and boundary conditions is shown in Figure 13c. With such shallow anchor installation it is likely that prior to the grout-soil interface failure, the soil mass in front of the anchor fails with the shear plans reaching the ground surface. Therefore, it is aimed here to verify this numerically, as part of the overall anchored

wall stability analysis.

Two anchor placement cases are considered: the anchor is positioned at $h$ and $2h$ distance away from the wall. The moment free connection of the anchor tie to the wall is implemented by overlapping it with soil/wall interface as was described previously. The tie itself does not interact with the soil to avoid its reinforcing effect, and has been modelled with the solid elements, but using moment-free joint conditions described in Section 3.3.

The resulting collapse patterns and the adapted meshes are given in Figure 16, with Figure 15b showing the moment-free/duplicated edges interface in action at collapse. The actual bounds of the gravity acceleration are summarised in Tables 6 and 7 for an anchor length equal to $h$ and $2h$, respectively. The interface conditions between the grouting and the soil are the same as for the wall/soil interface in all cases.

The effects of interface conditions are reflected in the power dissipation plots presented in Figure 16. In the smooth case, practically no dissipation is appearing at the wall/soil interfaces apart from that at the bottom of the wall (see Figure 16c). The collapse mechanism exhibits only one single failure line between the anchor and the top surface of the soil. Instead, when using the rough interface conditions, two failure lines are observed. This difference in collapse patterns is supported by the values in Table 6-7, which show a substantial reduction in the limit value of $d/h$ when the interface conditions are changed from rough to smooth.

The distance between the wall and the anchor is also a relevant parameter. While the limit values of $d/h$ increase when the distance is doubled, the mechanism is also qualitatively different. When the length equals $2h$, two independent failure areas are

| W/S Interface = rough | | | | W/S Interface = rough + NT | | | | W/S Interface = smooth | | | |
|---|---|---|---|---|---|---|---|---|---|---|---|
| $d/h$ | LB | UB | Err (%) | $d/h$ | LB | UB | Err (%) | $d/h$ | LB | UB | Err (%) |
| 0.794 | 0.874 | 0.987 | 6.072 | 0.794 | 0.857 | 0.969 | 6.134 | 0.606 | 0.858 | 0.967 | 5.973 |
| 0.788 | 0.905 | 1.022 | 6.072 | 0.788 | 0.887 | 1.004 | 6.187 | 0.600 | 0.881 | 0.997 | 6.177 |
| **0.781** | 0.936 | 1.058 | 6.118 | 0.781 | 0.918 | 1.039 | 6.183 | 0.594 | 0.905 | 1.023 | 6.120 |
| 0.775 | 0.968 | 1.094 | 6.111 | **0.775** | 0.949 | 1.075 | 6.225 | 0.588 | 0.930 | 1.047 | 5.918 |
| 0.769 | 1.000 | 1.131 | 6.147 | 0.769 | 0.981 | 1.112 | 6.259 | **0.581** | 0.956 | 1.081 | 6.136 |
| 0.763 | 1.032 | 1.169 | 6.224 | 0.763 | 1.013 | 1.149 | 6.290 | 0.575 | 0.982 | 1.112 | 6.208 |
| 0.756 | 1.065 | 1.208 | 6.291 | 0.756 | 1.047 | 1.187 | 6.267 | 0.569 | 1.011 | 1.139 | 5.953 |

Table 6: Limit values of the stability factor for different $d/h$ ratios of an anchored wall.

The anchor is placed at a distance $h$ from the wall and is $1$ meter long and $30cm$ wide.

| W/S Interface = rough | | | | W/S Interface = rough + NT | | | | W/S Interface = smooth | | | |
|---|---|---|---|---|---|---|---|---|---|---|---|
| $d/h$ | LB | UB | Err (%) | $d/h$ | LB | UB | Err (%) | $d/h$ | LB | UB | Err (%) |
| 0.838 | 0.769 | 0.915 | 8.670 | 0.825 | 0.834 | 0.991 | 8.603 | 0.638 | 0.872 | 1.031 | 8.355 |
| 0.831 | 0.802 | 0.955 | 8.708 | 0.819 | 0.870 | 1.032 | 8.517 | 0.631 | 0.893 | 1.062 | 8.645 |
| 0.825 | 0.837 | 0.995 | 8.624 | 0.813 | 0.907 | 1.075 | 8.476 | **0.625** | 0.914 | 1.087 | 8.646 |
| 0.819 | 0.873 | 1.036 | 8.539 | **0.806** | 0.945 | 1.119 | 8.430 | 0.619 | 0.936 | 1.108 | 8.415 |
| **0.813** | 0.910 | 1.079 | 8.497 | 0.800 | 0.984 | 1.164 | 8.380 | 0.613 | 0.959 | 1.141 | 8.667 |
| 0.806 | 0.948 | 1.123 | 8.450 | 0.794 | 1.024 | 1.211 | 8.367 | 0.606 | 0.982 | 1.170 | 8.736 |
| 0.800 | 0.987 | 1.168 | 8.399 | 0.788 | 1.065 | 1.255 | 8.190 | 0.600 | 1.008 | 1.196 | 8.530 |

Table 7: Limit values of the stability factor for different $d/h$ ratios of an anchored wall.

The anchor is placed at a distance $2h$ from the wall and is $1$ meter long and $30cm$ wide.

| Wall Type | Maximum stability ratio ($d/h$) | | | |
|---|---|---|---|---|
| | FEM [31] | Experimental | Computed [2] | Present work |
| Free standing wall | 0.62 | 0.60 | 0.55 | 0.600 |
| Simply supported wall | 0.81 | 0.80 | 0.73 | 0.85 |
| Anchored wall | 0.75 | 0.70 | 0.73 | 0.775 |

Table 8: Maximum stability ratios $d/h$ obtained for different retaining wall types and methodologies. The values for the present work are taken with a rough wall/soil interface with no traction and length of the anchor $= h$. The other values have been extracted from [31].

generated: one surrounding the rigid wall, and another at the top of the anchor.

The stability factors obtained for the retaining wall have been compared with those reported in [31], p. 149. Table 8 presents the details of the comparison, where the results obtained here are for a rough wall/soil interface with no-tension (which are the ones that were found to match better the reported results, as no detailed information on interface conditions used in [31] have been provided).

# 5 Conclusions

Modelling of interfaces and joints in the framework of computational limit analysis has allowed us to obtain pull-out capacities of anchors and stability limits of multi-anchored walls. The formulation presented has been verified so far on two-dimensional cases, but the methodologies described are equally applicable to general three-dimensional

problems.

Moreover, other geometrical configurations of the anchored wall such as multiple or non-horizontal anchors can be also analysed using the methods presented here. The cases treated in this paper are have been limited by belled passive (“dead”) anchors, i.e. those that are not pre-stressed. However, the inclusion of active anchors can be foreseen by adding the necessary initial pre-stress in the anchor system. Although the distribution of this stress may be non-trivial, the subsequent computational analysis poses no major theoretical difficulties. Therefore, it is suggested to pursue in the future the studies of active and other anchor types such as expandable rock anchors.

The focus of this paper has been on anchor/wall systems, but the limit analysis extensions described here are also applicable to the other systems such as slope stability, tunnel stabilisation, or securing of caverns. The examples analysed have demonstrated that formulations that preserve the strictness of the bounds are efficient for not only classical academic problems, but more importantly for the problems of practical interest.

# 6 Acknowledgements

The authors acknowledge the Spanish Ministry of Science and Innovation (MICINN) for its financially support through its mobility program to A Lyamin during his stay at the Department of Applied Mathematics III at UPC. Also, J J Munoz acknowledges A Modaressi at Ecole Centrale Paris for her fruitful discussions.

# References


[1] AD Bastable. Multibell ground anchors in London clay. In *Proc. 7th FIP cong. Tech. Session on Prest. Concrete Found. and Ground Anchors*, pages 33–37, New York, 1974.

[2] J Brinch-Hansen. *Earth pressure calculation*. Danish Technical Press, Cphenhagen, Denmark, 1953.

[3] F Cai and K Ugai. Reinforcing mechanism of anchors in slopes: a numerical comparison of results of lem and fem. *Int. J. Num. Anal. Meth. Geomech.*, 27(27):549–564, 2003.

[4] W F Chen. *Limit analysis and soil plasticity*. Dev. in Geoth. Engin. 7. Elsevier, 1975.

[5] E Christiansen. *Handbook of Numerical Analysis, vol IV*, volume IV, chapter II, Limit Analysis of Collapse States, pages 193–312. North Holland Amsterdam, 1996.

[6] H Ciria, J Peraire, and J Bonet. Mesh adaptive computation of upper and lower bounds in limit analysis. *Int. J. Num. Meth. Engng.*, 75:899–944, 2008.

[7] con J Salen˙ *Calcul à la rupture et analyse limite*. Presses de l'École Nationale des Ponts et Chaussées, 1991.

[8] KM Kouzer and Kumar. Vertical uplift capacity of two interfering horizontal anchors in sand using an upper bound limit analysis. *Comp. Geotech.*, 36:1084–1089, 2009.

[9] K Krabbenhøft, A V Lyamin, and S W Sloan. Formulation and solution of some plasticity problems as conic programs. *Int. J. Solids Struct.*, 44:1533–1549, 2007.

[10] J Kumar and KM Kouzer. Vertical uplift capacity of horizontal anchors using upper bound limit analysis and finite elements. *Can. Geotech. J.*, 45:698–704, 2008.

[11] X Li, S He, and Y Wu. O Lieleg and KM Schmoller and CJ Cyron and Y Luan and WA Wall and AR Bausch",. *Int. J. Num. Anal. Meth. Geomech.*, 2011.

[12] A V Lyamin. Sonic. Solver for second order conic programing. 2004.

[13] A V Lyamin, K Krabbenhøft, S W Sloan, and M Hjiaj. An adaptive algorithm for upper bound limit analysis using discontinuous velocity fields. In *Proceedings of European Congress on Computational Methods in Applied Sciences and Engineering, ECCOMAS 2004*, Jyväskylä, finland, 24-28 July 2004.

[14] A V Lyamin, S W Sloan, K Krabbenhøft, and M Hjiaj. Lower bound limit analysis with adaptive remeshing. *Int. J. Num. Meth. Engng.*, 63:1961–1974, 2005.

[15] A Makrodimopoulos and C M Martin. Upper bound limit analysis using simplex strain elements and second-order cone programming. *Int. J. Num. Anal. Meth. Geomech.*, 31(6):835–865, 2007.

[16] A Makrodimopoulos and C M Martin. Upper bound limit analysis using discontinuous quadratic displacement fields. *Comm. Num. Meth. Engng.*, 24:911–927, 2008.

[17] RS Merifield, AV Lyamin, SW Sloan, and HS Yu. Three-dimensional lower bound solutions for stability of plate anchors in clay. *J. Geoth. Geoenv. Engin.*, 129(3):243–253, 2003.

[18] RS Merifield, SW Sloan, and HS Yu. Stability of plate anchors in undrained clay. *Géotechnique*, 51(2):141–153, 2001.

[19] J J Muñoz, J Bonet, A Huerta, and J Peraire. Upper and lower bounds in limit analysis: adaptive meshing strategies and discontinuous loading. *Int. J. Num. Meth. Engng.*, 77:471–501, 2008.

[20] American Society of Civil Engineers. *Retaining and flood walls*, volume 4. ASCE Press, 1994.

[21] US Army Corps of Engineers. *Design of Sheet Pile Walls*, volume 110-2-2504 of *Engineer Manual*. Dep. of the Army, 1994.

[22] H Ostermayer. Construction carrying behavior and creep characteristics of ground anchors. In *ICE Conf. on Diaphragm Walls and Anchorages*, pages 141–151, London, 1974.

[23] H Ostermayer and T Barley. *Geotechnical Engineering Handbook, Procedures*, volume 2, chapter Ground Anchors, pages 169–215. Ernst & Sohns Verlag, 2003.

[24] H Ostermayer and F Sheele. Research on ground anchors in non-cohesive soils. *Revue Fran. Geoth.*, 3:92–97, 1978.

[25] J Pastor. Analyse limite: détermination numérique de solutions statiques completes. Application au talus vertical. *J. Méc. Appl.*, 2:167–196, 1978.

[26] S Plumey, A Muttoni, L Vulliet, and V Labiouse. Analytical and numerical analyses of the load-bearing capacity of retaining walls laterally supported at both ends. *Int. J. Num. Anal. Meth. Geomech.*, 35:1019–1033, 2011. DOI: 10.1002/nag.942.

[27] P W Rowe. Anchored Sheet-Pile Walls. *Proc. Inst. Civil Eng.*, 1(5788):27–70, Jan. 1952.

[28] P W Rowe. Sheet-Pile Walls at Failure. *Proc. Inst. Civil Eng.*, 5(6107):276–315, May 1956.

[29] J F Sturm. Using SeDuMi 1.02, a MATLAB toolbox for optimization over symmetric cones. *Optimization Methods and Software*, 11–12:625–653, 1999. Version 1.05 available from `http://http://sedumi.ie.lehigh.edu`.

[30] R H Tütüncü, KC Toh, and MJ Todd. Solving semidefinite-quadratic-linear programs using SDPT3. *Mathem. Progr. Ser. B*, 95:189–217, 2003. Avail. http://www.math.nus.edu.sg/ mattohkc/sdpt3.html.

[31] K C Vossoughi. *Étude numérique du comportement des ouvrages de soutènement à la rupture*. PhD thesis, Ecole Centrale Paris, Paris, France, 2001.

[32] P P Xanthakos. *Ground anchors and anchored structures*. J Wiley, 1991.

[33] L Yu, J Liu, XJ Kong, and Y Hu. Numerical study on plate anchor stability in clay. *Géotechnique*, 61(3):235–246, 2011.

[34] N Zouain, Herskovits J, L A Borges, and Feijóo RA. An iterative algorithm for limit analysis with nonlinear yield functions. *Int. J. Solids Struct.*, 30:1397–1417, 1993.

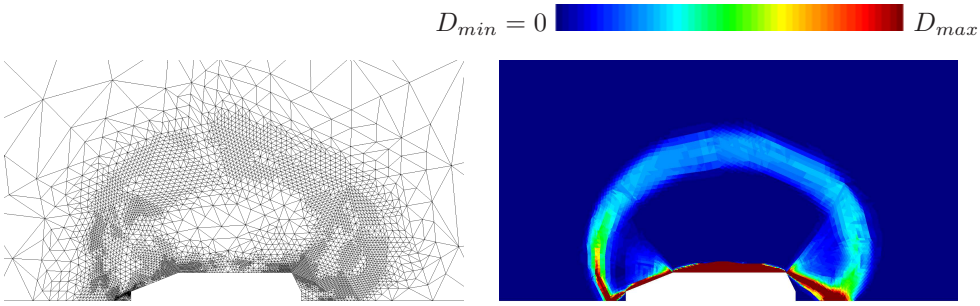


(b) Single-bell anchor. Clay soil with rough interface ($D_{max} = 150$).

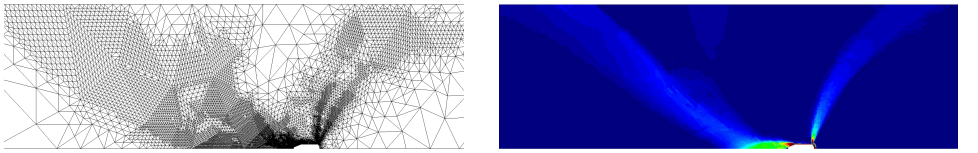

(c) Single-bell anchor. Sand ($\phi = 40°$) with rough interface ($D_{max} = 0.1$).

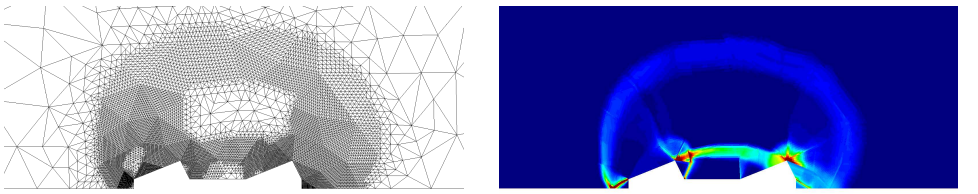

(d) Double-bell anchor. Clay soil with rough interface ($D_{max} = 500$).

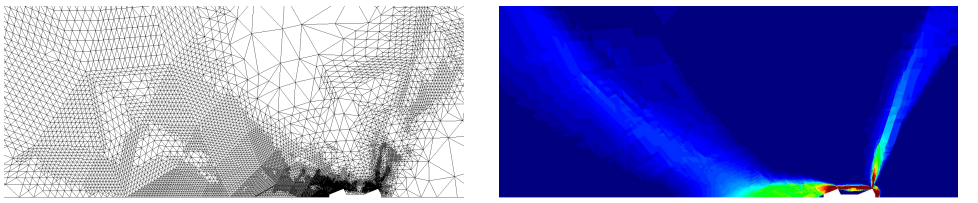

(e) Double-bell anchor. Sand ($\phi = 40°$) with rough interface ($D_{max} = 0.1$).

Figure 11: Detail of the final meshes (left) and dissipation power (right) for single- and double-bell anchors. For clarity, the anchor and the tie have been removed from the figures.

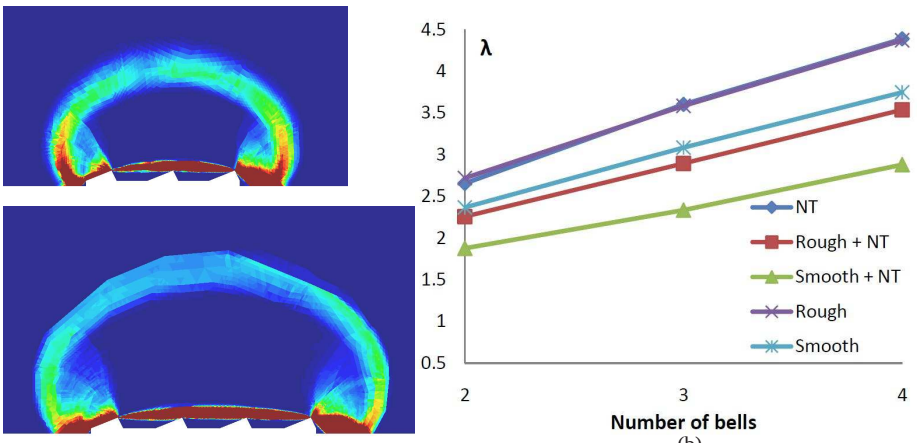


(a) (b)

Figure 12: (a): Contour plots of the dissipation power in clay soil using three and four bell anchors and rough interface. For clarity the anchors and the ties have been removed from these figures. (b): pull-out capacity of anchors in clay as a function of the number of bells for different interface conditions.

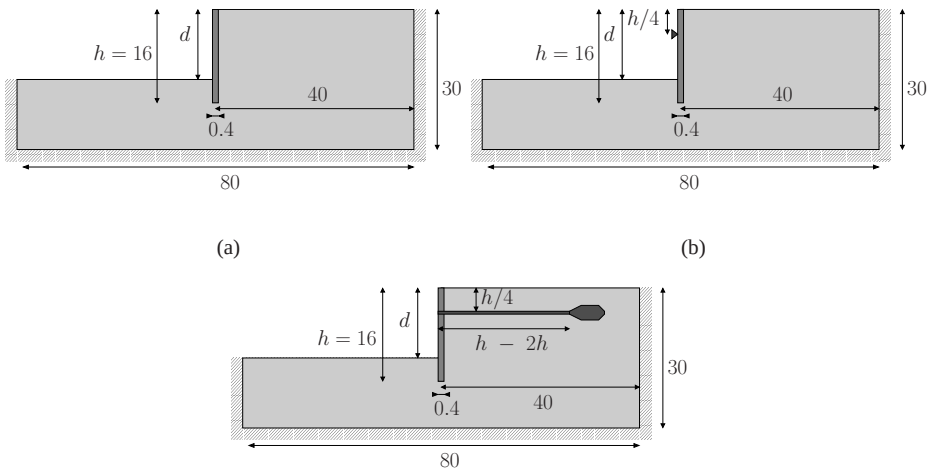


(a) (b)

(c)

Figure 13: Dimensions and boundary conditions of free standing (a), simply supported (b) and an anchored wall (c).

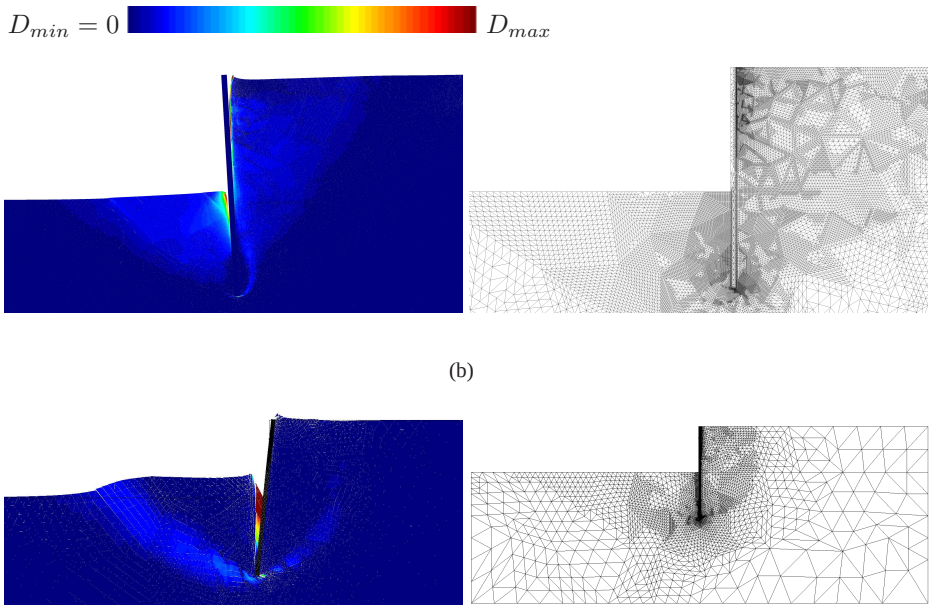


(b)

(c)

Figure 14: Dissipation power (left column) and meshes after adaptive process (right) of free standing wall, $D_{max} = 0.025$ (a) and simply supported wall (b). In both cases the wall/soil interface is rough + no tension, $D_{max} = 0.1$.

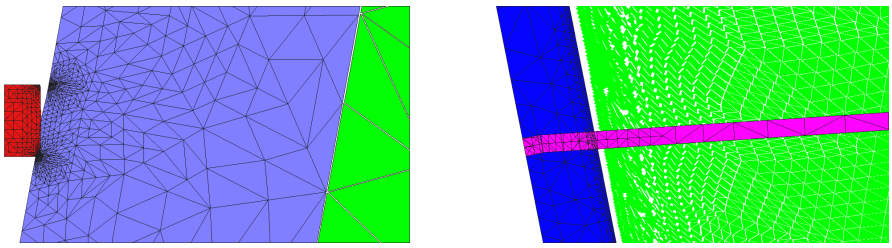

(a) (b)

Figure 15: (a): Detail of the rigid block (red, left) connected to the wall (blue) through a joint in the simply supported wall. (b): Detail of the anchor/wall connection with a duplicated edge at the left side and a joint in the tie, when using a wall/soil interface with rough+no tension condition (notice the wall/soil separation, while the wall/achor connection stays intake).

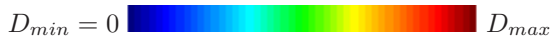


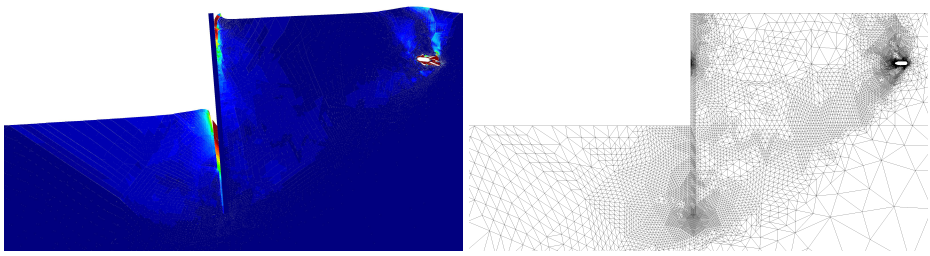

(b) Anchored wall with no traction at interfaces, length of anchor $= h$, $D_{max} = 0.5$.

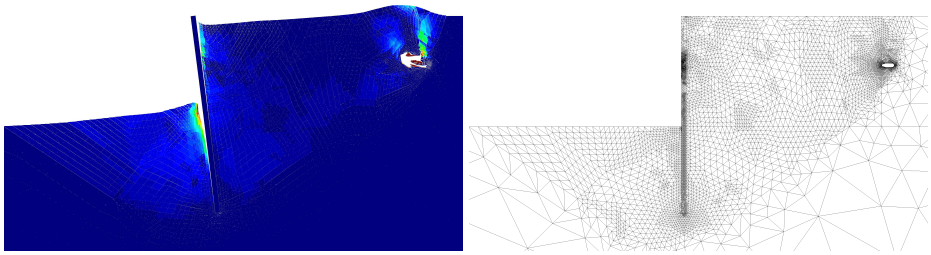

(c) Anchored wall with rough interfaces, length of anchor $= h$, $D_{max} = 0.1$.

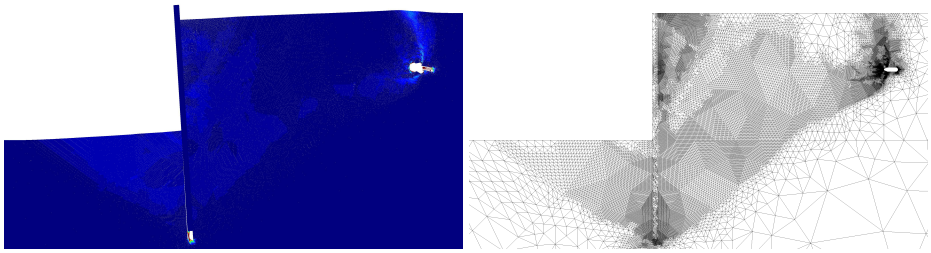

(d) Anchored wall with smooth interfaces, length of anchor $= h$, $D_{max} = 0.1$.

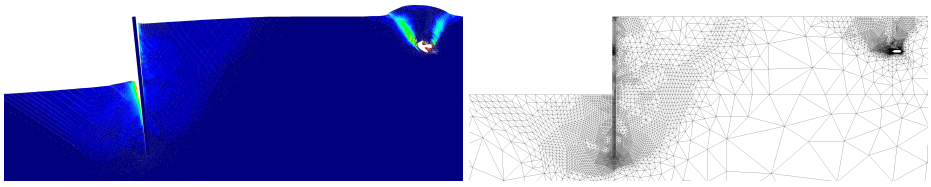

(e) Anchored wall with rough interfaces, length of anchor $= 2h$, $D_{max} = 0.1$.

Figure 16: Anchored wall. Dissipation energy (left column) and meshes after adaptive process (right).